J Mater Sci (2007) 42:660–668
DOI 10.1007/s10853-006-1137-x

Unusual magnetic and transport properties of the CMR $Pr_{1-x}Ca_xMnO_{3-y}$ system

Ri-Zhu Yin · Chul Hyun Yo

Received: 16 October 2003 / Accepted: 17 November 2005 / Published online: 18 November 2006

Abstract The substituted nonstoichiometric perovskite $Pr_{1-x}Ca_xMnO_{3-y}$ compounds have been synthesized by a standard combustion technique, which show uniphase solid solutions. The all samples of the $Pr_{1-x}Ca_xMnO_{3-y}$ system show an orthorhombic crystal system and the cell volumes are decreased with increasing the larger amounts of substituted atoms or the increasing x values. The mixed valence of Mn ions is identified by the XAS (XANES/EXAFS) spectroscopy and the amounts of Mn^{4+} ions are determined by an iodometric titration method. Nonstoichiometric chemical formulas of the $Pr_{1-x}Ca_xMn^{3+}_{1-\tau}Mn^{4+}_{\tau}O_{3-y}$ compounds have been obviously formulated. Magnetic properties are investigated by SQUID and thus the $Pr_{1-x}Ca_xMnO_{3-y}$ ($x = 0.4$, 0.6, and 0.8) compounds show the transition from antiferromagnetic state to paramagnetic state. The $Pr_{1-x}Ca_xMnO_{3-y}$ ($x = 0.0$, 0.2, and 1.0) compounds show the transition from ferromagnetic state to paramagnetic state. The facts that Mn^{4+} contents play important roles in the magnetic ordering have been found out. The transport properties have been studied by the DC electrical conductivity measurement under magnetic fields of 0 G and 3 kG. Maximum and minimum MR ratios are 1016% of the $Pr_{0.6}Ca_{0.4}MnO_{2.846}$, and –77.5% of the $PrMnO_{3.021}$ compound, respectively.

R.-Z. Yin · C. H. Yo
Department of Chemistry, Yonsei University, Seoul 120-749, South Korea

C. H. Yo (✉)
Korea Institute of Science and Technology Information, 206-9, Cheonnyangni-dong, Dongdaemun-gu, Seoul 130-741, South Korea
e-mail: chulhyun@yonsei.ac.kr

Introduction

The magnetoresistive effect describes the phenomenon whereby the electrical resistivity of a solid changes with an application of a magnetic field. An interest in this effect, first observed by Kohler in 1938 [1] and later by Volger in 1950s [2], has been stimulated by the observation of large values of magnetoresistance (MR) in metallic multilayered thin films [3, 4].

Widespread interests in the chemistry, physics, and materials science communities have been kindled when even larger values of MR were found in $Ln_{1-x}A_xMnO_3$ perovskite system, where A is an alkali-earth cation or an alkali cation and Ln is a trivalent lanthanide cation. The MR in these compounds has been first observed in thin films [5–7] but later shown even in bulk samples [8, 9].

Relationships between composition/structure and properties of ABO_3 perovskites are usually parametrized using the formal oxidation state of the transition metal and the tolerance factor. The oxidation state describes the number of electrons available to fill the energy bands and the tolerance factor parametrizes structural effects due to the average size of A site and B cations. However, the recent explosion of interest in the manganite perovskites has shown these two parameters [10].

The manganese oxides known to be high magnetoresistance materials are derived from chemical doping of insulators. The local moments that are ordered in the doped materials already exist in the insulator and thus with a first approximation, the metallicity and magnetism are independent properties [11].

The electrical resistance is reduced when there is less scattering of the conduction electrons by the spins

of the localized electrons. To the extent that an external magnetic field reduces the disorder among the local spin states, the scattering will be reduced, resulting in a negative magnetoresistance. By contrast, the electrical carriers are expressed more scattering action which is induced by magnetic field bending effect, resulting a positive magnetoresistance. The lattice spin ordering competed with the carrier scattering [12].

In the present study, the relationship between local structures/electronic states and physical properties such as magnetic and transport properties are widely discussed. Especially, the discussions are focused on the relationship between microstructures and macroproperties.

Experimental section

All the samples have been synthesized by standard combustion techniques. Appropriate amounts of Mn_2O_3 (Aldrich, 99.9%), $Pr(CH_3COO)_2$ (Strem, 99.9%), and $CaCO_3$ (Aldrich, 99.9%) are mixed and grinded together with ethanol in a mortar. The mixtures are heated at 800 °C for 8 h and then grinding about 2 h, the powder put in ceramic boat and sintered at 1150 °C for 24 h. The grinding and sintering steps are repeated until the uniphase solid solutions are obtained.

All XRD patterns of the samples are recorded by Rigaku X-ray diffractometer at room temperature. The X-ray diffraction data have been analyzed by using Rietveld's powder diffraction profile-fitting technique with cerius 2 (version 3.5, with DBWS, S. G. Inc.) to determine the crystallographic information such as lattice parameters and atomic positions, etc.

Mn K-edge X-ray absorption spectra (XAS) have been recorded on the BL3C1 beam line of Pohang Light Source (PLS) with the storage ring current of 120–150 mA at 2.03 GeV. Magnetic properties of the samples are investigated by the SQUID (Quantum Design Magnetic Property Measurement System, San Diego, CA). The measurements are carried out in the temperature range of 5–300 K in an applied field of 1 Tesla.

The samples are pressed to a pellet with 3 ton/cm^2 pressure and quenched from the same sintering temperature for 1 day. Electrical DC resistance measurements are carried out from 100 K to room temperature by the four-probe method using Keithley SMU 238 Model. The DC resistances are also measured under magnetic field of 3 kG in the same temperature range. The mixed valence between Mn^{3+} and Mn^{4+} ions has been determined by the iodometric titration method [13].

Results and discussion

Structural properties

The X-ray patterns of the samples at room temperature show a good solid solution with a single phase as shown in Fig. 1. Rietveld refinement of these models gives a satisfactory fits to the overall profile. The typical best-fit of XRD patterns of samples are shown in Fig. 2. All of the samples are exhibited orthogonally distorted perovskite structure with dimensions.

The effective ionic radii of the Pr^{3+} with 9 coordinates, Ca^{2+} with 12 coordinates, Mn^{3+} with 6 coordinates, and low spin O^{2-} with 2 coordinates are 132, 148, 72, and 121 pm, respectively. The tolerance factor [14] t of this system is in the range of 0.927–0.986. The fractional coordinates of the $Pr_{1-x}Ca_xMnO_{3-y}$ system at room temperature are listed in Table 1 from Rietveld refinements. Refinement processes are carried out with several variations such as baseline correction, cell parameters, zero correction, scale factor, temperature factor, etc. All of the compounds are assigned to the orthorhombic system with *Pnma* space group.

The cell volumes are decreased with the increasing Ca content instead of the Pr ions or the x values. It can be explained that the larger A site Ca cations play an distortion factor for the system. The lattice distortion, lead to Mn-O bond length variation, and Mn–O–Mn bond angle change. The crystallographic data of the $Pr_{1-x}Ca_xMnO_{3-y}$ system are listed in Table 2.

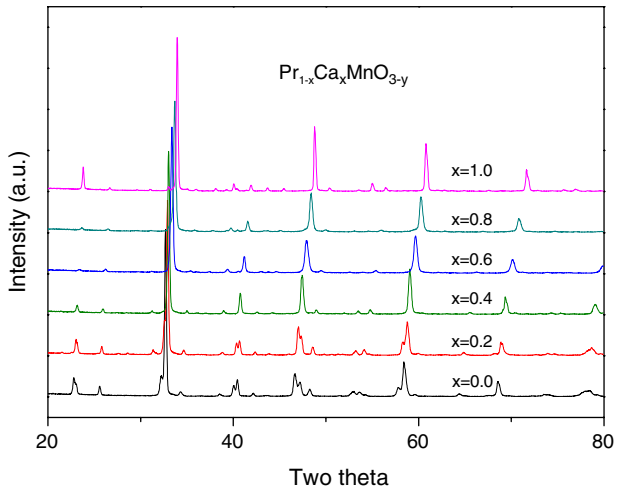

Fig. 1 The XRD patterns of the $Pr_{1-x}Ca_xMnO_{3-y}$ system

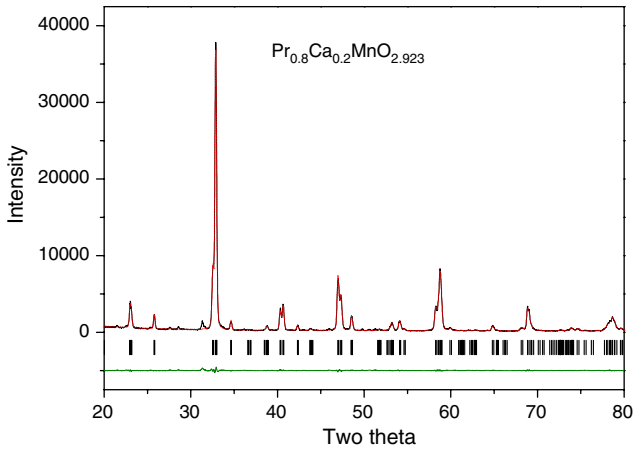

Fig. 2 Experimental, simulated, the difference, and Bragg reflection profiles after the Rietveld refinement of the $Pr_{1-x}Ca_xMnO_{3-y}$ system: the typical one of the samples

Table 1 Fractional coordinates of the $Pr_{1-x}Ca_xMnO_{3-y}$ system at room temperature

Atom	*x*	*y*	*z*
Pr(Ca)	0.0273	0.25	–0.0072
Mn	0	0	0.5
O	0.4873	0.25	0.854
O	0.3034	0.0257	–0.2442

More detailed information from Rietveld refinement such as Mn–O bond lengths, Mn–O–Mn bond angles of the $Pr_{1-x}Ca_xMnO_{3-y}$ system at room temperature are also presented in Table 3. The lattice distortion is easily observed by the crystal system induced from the ideal cubic to orthorhombic system. The cell volumes are decreased with decreasing mean bond length of the Mn–O.

The X-ray absorption spectra are calibrated with standard Mn metal foil. The normalized Mn K-edge XAS (XANES/EXAFS) spectra are shown in Fig. 3. The absorption coefficient is rapidly increased at 6558 eV for the Mn K-edge absorption energy. The strong absorption peak at 6558 eV is induced from dipole allowed 1s $\rightarrow$ 4p transition and the weak quadrupole-allowed 1s $\rightarrow$ 3d transition also has been observed.

The information of local structure such as bond lengths, coordinate numbers, and Debye–Waller factors will be obtained from the whole range fitting of the XAS spectrum. However, the fitting of EXAFS is impossible since the Pr L_I(6846 eV) edge and the Mn K(6539 eV) edge are almost overlapped. In order to obtain more clear XANES spectra, the second derivative spectra have been shown in Fig. 4.

In Fig. 4, the A peak assigns to the transition of 1s electron to an unoccupied 3d orbital, which corresponds to the electric-dipole forbidden transition under the selection of $\Delta l = \pm 1$. Under the octahedral crystal field symmetry the bound state of Mn^{4+} ion in the sample presents $3d^3$ ($t_{2g}^3 e_g^0$) state, the probability of transition to the t_{2g} and e_g or $A_1(t_{2g})/A_2(e_g)$ peak area ratio is 3:4. The bound state of Mn^{3+} ion in the sample presents $3d^4$ ($t_{2g}^3 e_g^1$) state at high spin and $3d^4$ ($t_{2g}^4 e_g^0$) state at low spin, which are corresponding to the peak area ratios of 1:1 and 1:2, respectively. The experimental $A_1(t_{2g})/A_2(e_g)$ value is lying from 0.5 to 0.75. If Mn^{3+} high spin state is exist in the system, the area ratio value should be greater than 0.75. It means that Mn^{3+} ions are favor to stay in low spin state.

The energy difference between t_{2g} and e_g states, or 10 Dq, corresponds to about 2.1 eV from the degree of the peak splitting. The 10 Dq value gradually decreased with the increasing Ca content in the $Pr_{1-x}Ca_xMnO_{3-y}$ system. The fact is good agreement with more Mn 3d and O 2p orbital mixing, which gives rise to shorter mean Mn–O bond length. The peak positions and the area ratios are listed in Table 4.

Table 2 Refinement statistics and structural parameters of the $Pr_{1-x}Ca_xMnO_{3-y}$ system at room temperature

Parameter	Composition (*x*)					
	0.0	0.2	0.4	0.6	0.8	1.0
R_{wp} (%)	14.13	11.54	11.12	9.88	13.27	13.90
R_p (%)	9.29	7.19	7.36	7.07	9.25	8.14
Wavelength (Å)	1.5418	1.5418	1.5418	1.5418	1.5418	1.5418
2θ range (°)	20–80	20–80	20–80	20–80	20–80	20–80
Space group	*Pnma*	*Pnma*	*Pnma*	*Pnma*	*Pnma*	*Pnma*
a (Å)	5.431	5.381	5.381	5.370	5.363	5.276
b (Å)	7.728	7.583	7.576	7.568	7.579	7.451
c (Å)	5.417	5.368	5.365	5.379	5.361	5.263
Volume (Å^3)	227.37	219.04	218.73	218.61	217.91	206.90
Mean Mn–O bond length[a]	1.922	1.899	1.898	1.897	1.896	1.863

[a] The mean Mn–O bond length is calculated from lattice parameter as an average value of $\frac{a}{2\sqrt{2}}$, $\frac{b}{4}$, and $\frac{c}{2\sqrt{2}}$

Table 3 Mn–O bond lengths, and Mn–O–Mn bond angles of the $Pr_{1-x}Ca_xMnO_{3-y}$ system at room temperature

x value	Bond lengths (Å) Mn–O	Bond angles (°) Mn–O–Mn
0.0	2.250	4 × 162.5
	1.630	2 × 142.1
	2.043	
0.2	2.044	4 × 155.1
	1.919	2 × 159.6
	1.953	
0.4	2.099	4 × 164.1
	1.737	2 × 158.4
	1.928	
0.6	2.139	4 × 161.9
	1.708	2 × 165.3
	1.908	
0.8	2.138	4 × 163.8
	1.693	2 × 134.9
	2.051	
1.0	1.978	4 × 156.8
	1.826	2 × 157.1
	1.901	

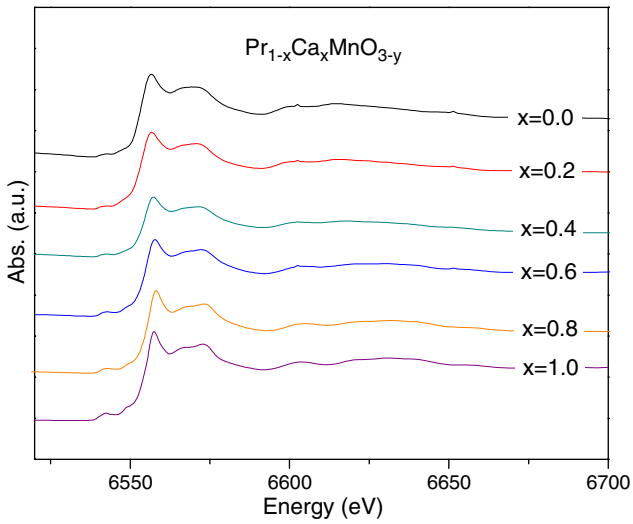

Fig. 3 The Mn K-edge XAS spectra of the $Pr_{1-x}Ca_xMnO_{3-y}$ system

The absorption shoulder B peak can be assigned to the peak of shake up/shake down process. The shake down process is usually more affected by the Mn ion oxidation state rather than the local structure. The main absorption peak C or white line at about 6556.8 eV represents the 1s → 4p electric dipole allowed transition. The absorption C peak is blue shifted with the increasing x value in the $Pr_{1-x}Ca_xMnO_{3-y}$ system. The shift is also good agreement with the shorter mean bond length of Mn–O in the $Pr_{1-x}Ca_xMnO_{3-y}$ system. The shorter bond length leads

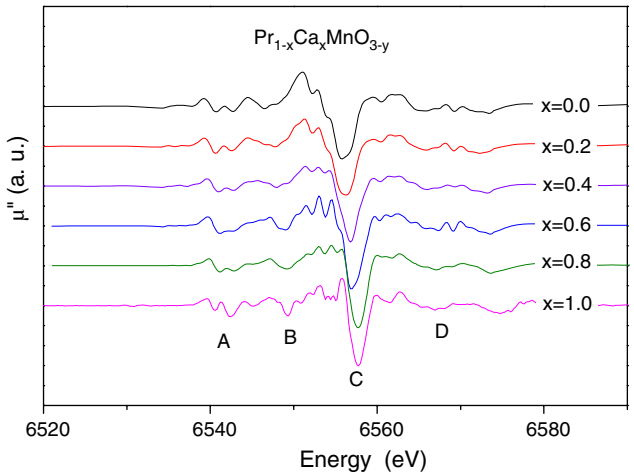

Fig. 4 The second derivative XANES spectra of the $Pr_{1-x}Ca_xMnO_{3-y}$ system

to increase the bond covalency and the high covalent state increases the energy level state, resulting the high-energy shift.

Nonstoichoimetry

The iodometric titrations have been carried out in order to determine the contents of Mn^{3+} and Mn^{4+} ions (τ value) in the $Pr_{1-x}Ca_xMnO_{3-y}$ system. There are two proposed mechanisms to keep the charge neutrality in the compounds. The one forms the Mn^{4+} ion to compensate the doped lower valency cation and the other forms the oxygen vacancy or the nonstoichiometry. Jonker et al. reported that the first the mechanism is predominant when small mount of alkali earth metal is doped and the second is superior when the doped content is over 50% [15].

The *x*, τ, *y* values and nonstoichiometrical chemical formula of the $Pr_{1-x}Ca_xMn^{3+}{}_{1-\tau}Mn^{4+}{}_{\tau}O_{3-(x-\tau)/2}$ system are listed in Table 5. The *y* value or oxygen contents are calculated from iodometrically determined τ and *x* value. The Mn^{4+} ion content or value increases with the *x* value in the system. The oxygen vacancy or nonstoichiometric composition (*y* value) also shows the same tendency. It is related to the synthetic conditions such as partial oxygen pressure, sintering temperature, preparation time, etc.

Magnetic properties

The magnetic properties can be usually classified to diamagnetism, paramagnetism, antiferromagnetism, ferrimagnetism and ferromagnetism. The magnetic

Table 4 Peak positions and area ratios of Mn K-edge XANES spectra for the $Pr_{1-x}Ca_xMnO_{3-y}$ system[a]

x value	A_1 peak (eV)	A_2 peak (eV)	10 Dq (eV)	A_1/A_2 (area)	B peak (eV)	C peak (eV)
0.0	6540.6	6542.8	2.2	0.734	6546.6	6555.8
0.2	6540.6	6542.7	2.1	0.690	6547.7	6556.3
0.4	6540.9	6542.9	2.0	0.584	6547.7	6556.8
0.6	6541.1	6542.9	1.8	0.506	6548.6	6557.0
0.8	6541.2	6542.9	1.7	0.619	6549.4	6557.6
1.0	6540.5	6542.5	2.0	0.553	6550.2	6557.8

[a] Each peak has been fitted with the Lorentzian function, $f(E) = 2A\Gamma/\pi\{\Gamma^2 + 4(E - E_c)^2\}$, where E, A, and Γ represent peak position, peak area, and full width at half maximum (FWHM) of the peak, respectively

Table 5 The x, τ, and y values and nonstoichiometric chemical formula for the $Pr_{1-x}Ca_xMnO_{3-y}$ system

x value	τ value	y value	Chemical formula
0.00	0.042	–0.021	$PrMn^{3+}_{0.958}Mn^{4+}_{0.042}O_{3.021}$
0.20	0.046	0.077	$Pr_{0.8}Ca_{0.2}Mn_{0.954}{}^{3+}Mn_{0.046}{}^{4+}O_{2.923}$
0.40	0.093	0.154	$Pr_{0.6}Ca_{0.4}Mn_{0.907}{}^{3+}Mn_{0.093}{}^{4+}O_{2.846}$
0.60	0.237	0.182	$Pr_{0.4}Ca_{0.6}Mn_{0.763}{}^{3+}Mn_{0.237}{}^{4+}O_{2.818}$
0.80	0.202	0.299	$Pr_{0.2}Ca_{0.8}Mn_{0.798}{}^{3+}Mn_{0.202}{}^{4+}O_{2.701}$
1.00	0.312	0.344	$CaMn_{0.688}{}^{3+}Mn_{0.312}{}^{4+}O_{2.656}$

Table 6 Transition temperatures T_N and T_C, effective magnetic susceptibility (μ_{eff}) and calculated μ_{eff} value from mixed valence of Mn ions for the $Pr_{1-x}Ca_xMnO_{3-y}$ system

x	T_N (K)	T_C (K)	μ_{eff} (obs.) (BM)	μ_{eff} (cal.) (BM)	Mn^{4+} spin	Mn^{3+} spin
0.0		122.0	2.430	2.874	High	Low
0.2		143.5	2.363	2.878	High	Low
0.4	167.6		2.589	2.927	High	Low
0.6	278.0		2.363	3.076	High	Low
0.8	181.9		2.254	3.040	High	Low
1.0		116.5	2.480	3.154	High	Low

Mn^{4+}: μ_{eff} = 3.87 BM, Mn^{3+}: μ_{eff} (high spin) = 4.90 BM, and Mn^{3+}: μ_{eff} (low spin) = 2.83 BM

susceptibilities χ of different kinds of magnetic materials are distinguished by their differences as well as by their absolute magnitudes.

The effective magnetic moment μ_{eff} is calculated from the linear part of the plot of χ_M^{-1} versus T for the $Pr_{1-x}Ca_xMnO_{3-y}$ system and listed in Table 6. Since only Mn ion of the sample has the unpaired electron, the magnetic susceptibility can be theoretically calculated. As listed in Table 6, Mn^{4+} and Mn^{3+} ions have been observed in the high and low spin states, respectively. It shows that the Mn d orbital electrons are not able to occupy the higher e_g band by the thermal excitation. The similar phenomena have also been observed in the $Pr_{1-x}Pb_xMnO_{3-y}$ system [16].

As shown in Fig. 5, it is easily observed that the compositions of $x = 0.0$, 0.2, and 1.0 for the $Pr_{1-x}Ca_xMnO_{3-y}$ have the transition from ferromagnetic to paramagnetic. The compositions of $x = 0.4$, 0.6, and 0.8 for the $Pr_{1-x}Ca_xMnO_{3-y}$ show the transition of antiferromagnetic to paramagnetic. The Neel temperatures of the compositions of $x = 0.4$, 0.6, 0.8 for the $Pr_{1-x}Ca_xMnO_{3-y}$ are related to the content of Mn^{4+} ion and thus higher T_N is present in larger amount of Mn^{4+} ions.

The antiferromagnetic behavior can be interpreted by a super-exchange effect as shown in Fig. 6. The Mn^{4+} ion has d^3 unoccupied electrons in high spin state, but the Mn^{3+} ion has d^4 electrons with two unpaired electrons in low spin state. In an octahedral symmetry, the effective Mn d orbital electrons are able to couple magnetically with O^{2-} 2p orbital electrons. The O^{2-} 2p orbitals have two electrons which all coupled antiparallel.

Thus, Mn and O ions are sufficiently close to couple their electrons and thus a chain coupling effect occurs through the whole crystal structure. The neighboring Mn ions separated by intervening O^{2-} ions are coupled antiparallel. Since the larger amount of Mn^{4+} ions lead to higher effective magnetic moment and long range magnetic ordering in the lattice, the antiparallel phase is easily kept until the ordering is thermally destroyed.

The compositions of $x = 0.0$, 0.2, and 1.0 of the $Pr_{1-x}Ca_xMnO_{3-y}$ system show the ferromagnetic ordering, which can be interpreted by double-exchange mechanism. The effective magnetic moments of the Mn ions are canted to emphasize the fluctuations in the orientation.

The effective magnetic moment is transferred to the bridging oxygen p orbital, which drives a spin-aligned electron from the oxygen p orbital to the empty Mn^{4+} orbital. The T_C of the $CaMnO_{2.656}$ compound is abnormally low, since very high oxygen defect and Mn^{4+} ion content result in some lattice variations which may reduce the magnetic ordering.

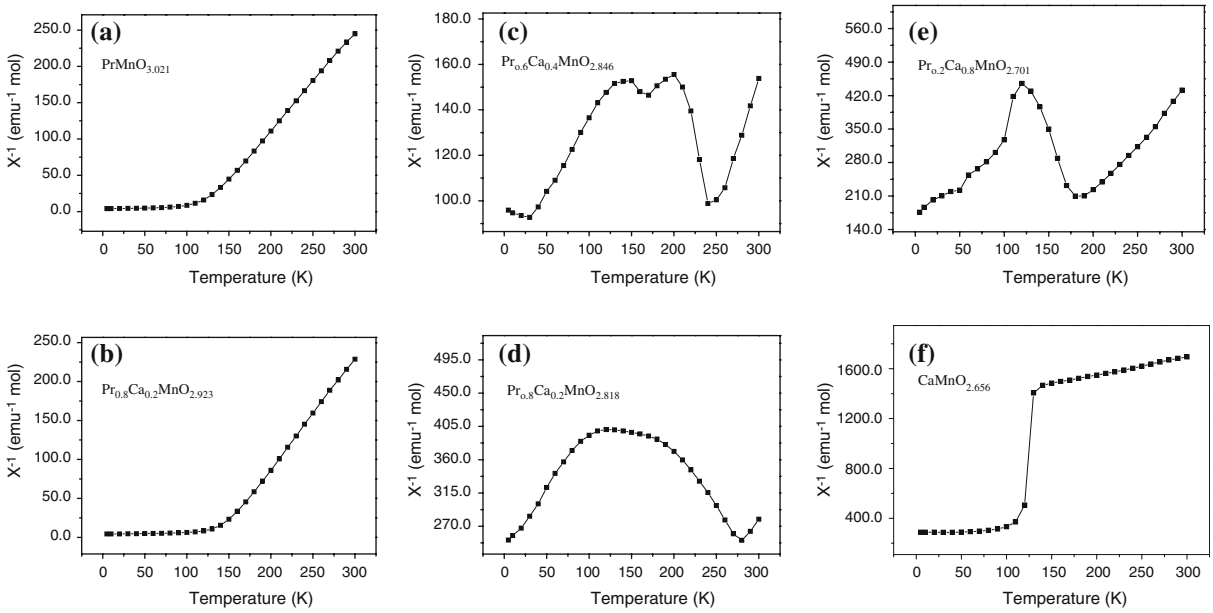

Fig. 5 Plots of χ_M^{-1} versus T for the $Pr_{1-x}Ca_xMnO_{3-y}$ system: (**a**) $x = 0.0$, (**b**) $x = 0.2$, (**c**) $x = 0.4$, (**d**) $x = 0.6$, (**e**) $x = 0.8$, and (**f**) $x = 1.0$

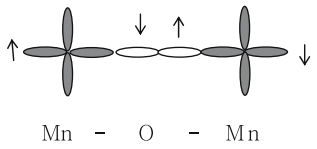

Fig. 6 Schematic diagram of the super-exchange process in the manganites where electron magnetic moments are present by arrows

Transport properties

The transport properties have been investigated by the electrical conductivity measurement with four probe method in the magnetic field of 0 G or 3 kG which is applied perpendicular to the sample. The DC potential (V) and electric current (I) are measured separately and simultaneously and then the electrical conductivity (σ) is calculated by the Laplume equation [17].

The measured conductivities of the $Pr_{1-x}Ca_xMnO_{3-y}$ system are shown in the Arrhenius plot of log σ versus $1000/T_{CO}$ in Fig. 7. The activation energy has been calculated from the slope of the Arrhenius plot by the following equation:

$$\sigma = \sigma^0 \exp(-E_a/RT) \quad \text{or} \quad \log \sigma = \log \sigma^0 - E_a/(2.303RT)$$

The observed charge ordered transition temperature under 0 G and 3 kG magnetic fields, the calculated activation energy, and the MR ratio are listed in Table 7:

$$\text{MR ratio}\,(\%) = [(R_H - R_0)/R_0] \times 100\%$$

where R_H and R_0 are the resistances of the sample under 3 kG and 0 G magnetic fields, respectively. The activation energies of the samples are in the range of 0.149–0.262 eV. The activation energy is significantly higher than the value of 0.121 eV measured by Jaime et al. on the thin film of the $La_{0.67}Ca_{0.33}MnO_3$ [18]. The high activation energy may be ascribed to the lower ordering state and grain boundaries.

The charge ordered transition temperature (T_{CO}) of the samples under a field of 3 kG is higher than that under zero magnetic field. Since the magnetic field application may induce a spin ordering increasing, thus the samples are more easily kept the charge ordered state under a magnetic field, so the T_{CO} value has been increased. The smallest negative and the largest positive magnetoresistances are observed in the $PrMnO_{3.021}$ with the value of –77.5%, and in the $Pr_{0.2}Ca_{0.8}MnO_{2.923}$ with that of 1016%, respectively.

The negative magnetoresistance is induced from the magnetic ordering of the sample. The ordered spin state plays a role of the increasing delocalization of the Mn–O–Mn lattice electrons. It is found out that the MR ratio is decreased by the increasing activation energy, since higher activation energy plays a role to magnify the magnetic field.

The positive magnetoresistance is induced by the changed path of electron carrier moving. The charged carrier is bended by the magnetic field to reduce the carrier mobility. The MR ratio is also decreased by

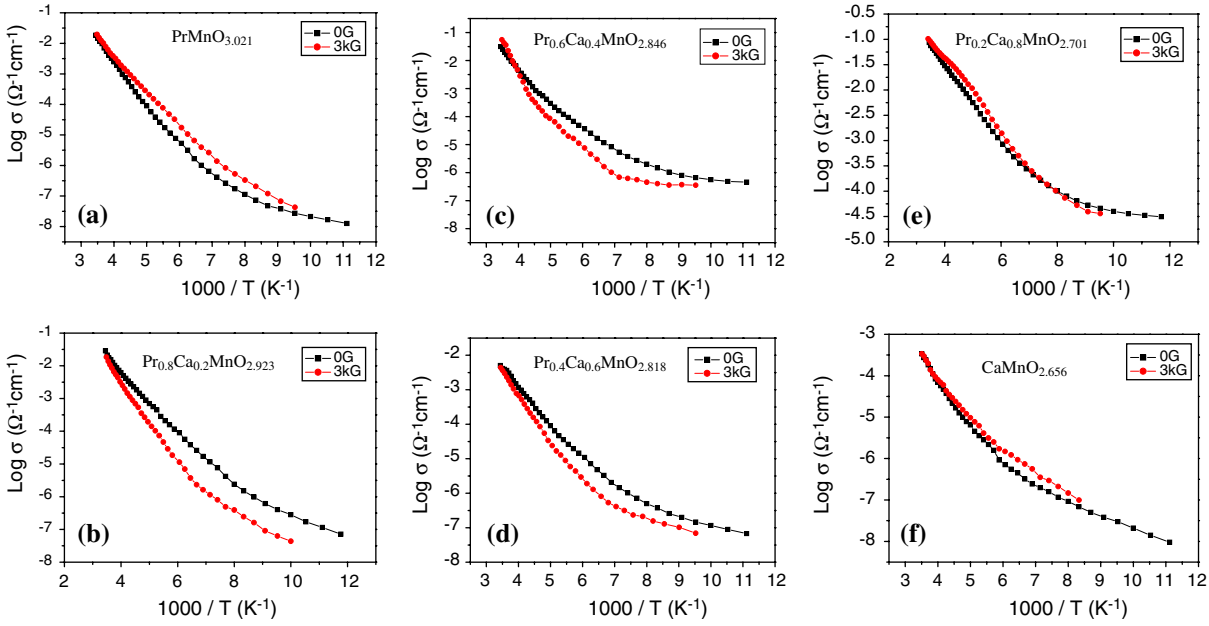

Fig. 7 Plot of log σ (electrical conductivity) versus 1000/T for the $Pr_{1-x}Ca_xMnO_{3-y}$ system: (**a**) $x = 0.0$, (**b**) $x = 0.2$, (**c**) $x = 0.4$, (**d**) $x = 0.6$, (**e**) $x = 0.8$, and (**f**) $x = 1.0$

Table 7 Transition temperatures T_{CO}, activation energy, and MR ratio of the $Pr_{1-x}Ca_xMnO_{3-y}$ system

x	T_{CO} (K)		E_a (eV)		MR_{max}	
	0 G	3 kG	0 G	3 kG	Ratio (%)	T (K)
0.0	126.6	141.4	0.048[a]	0.121[a]	–77.5	169.1
			0.262[b]	0.228[b]		
0.2	131.3	152.6	0.069[a]	0.105[a]	1016	148.5
			0.178[b]	0.232[b]		
0.4	136.0	155.4	0.034[a]	0.026[a]	711	150.1
			0.208[b]	0.272[b]		
0.6	140.1	164.8	0.048[a]	0.054[a]	285	161.3
			0.217[b]	0.280[b]		
0.8	132.5	147.8	0.017[a]	0.063[a]	–48.8	188.2
			0.149[b]	0.142[b]		
1.0			0.203	0.147	–56.5	156.2

[a] Below the T_{CO}

[b] Above the T_{CO}

the increasing activation energy, since the large activation energy hinders the carrier movement and the movement is relatively rare affected by the applied magnetic field. When $x = 0.2$, 0.4, 0.6 in the $Pr_{1-x}Ca_xMnO_{3-y}$ system, shows positive value of magnetoresistance. It is not so clear, may be due to the cation ordering state hindered the charged carrier's moving.

The temperature dependences of the MR ratios are shown in Fig. 8. The maximum MR ratio is observed at about the T_{CO} value in every samples. The MR ratio shows both positive and negative values because the positive bending effect and negative spin ordering one are comparable in the system.

The activation energies under the magnetic field and zero magnetic field of the same sample are different, since the tightly bounded Mn–O bond is easily affected by the external magnetic field. The activation energy value under the magnetic field is higher than that under zero magnetic field in the positive MR ratio. On the contrary, the activation energy is lowered in the negative MR ratio sample. It is good agreement with that the competitive two processes are taking placed in the system.

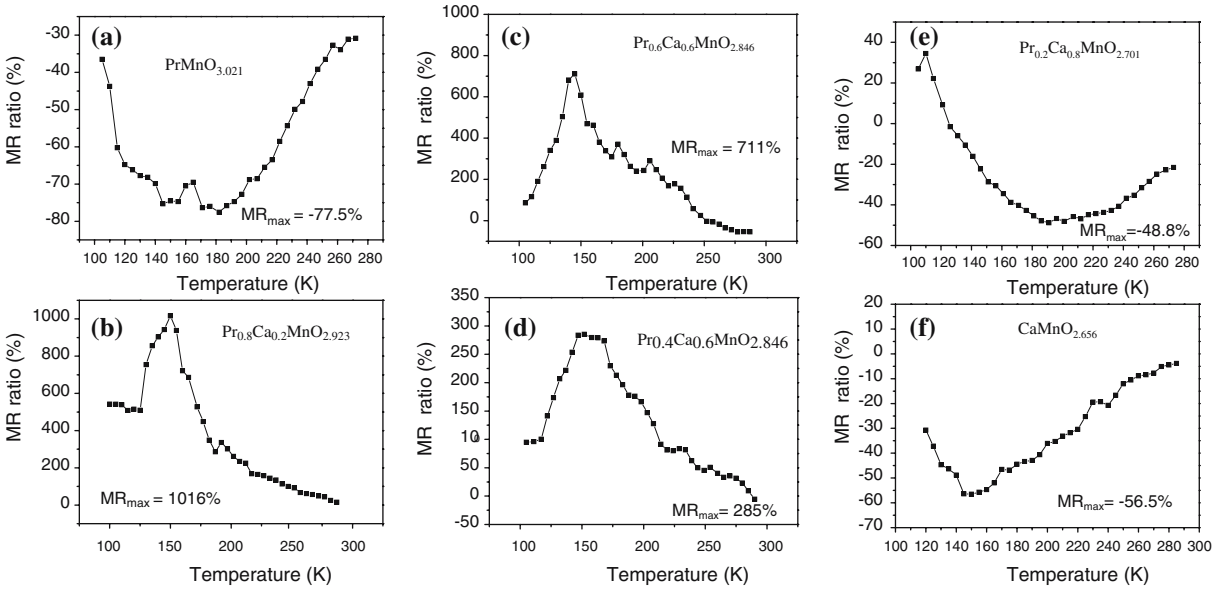

Fig. 8 The temperature dependent MR ratio for the $Pr_{1-x}Ca_xMnO_{3-y}$ system: (**a**) $x = 0.0$, (**b**) $x = 0.2$, (**c**) $x = 0.4$, (**d**) $x = 0.6$, (**e**) $x = 0.8$, and (**f**) $x = 1.0$

Conclusions

The magnetoresistive rare earth manganites exhibit a variety of properties and phenomena with an extraordinary sensitivity to various factors such as cations size, mixed valence of the Mn ion, structural distorted state, and magnetic and electric fields, etc. In particular, the mutual relations between charge ordering and spin ordering in the samples are truly fascinating.

The unique solid solutions of the $Pr_{1-x}Ca_xMnO_{3-y}$ ($x = 0.0$, 0.2, 0.4, 0.6, 0.8, and 1.0) system have been analyzed by XRD Rietveld refinement. All the samples of the $Pr_{1-x}Ca_xMnO_{3-y}$ system show orthorhombic crystal system with *Pnma* space group and the cell volumes are decreased with the larger substituted Ca^{2+} ion content or the x value.

The weak absorption peaks corresponding to the dipole-forbidden 1s $\rightarrow$ 3d transition appear at a pre-edge region of about 6541 eV on the Mn K-edge XANES spectra. The peak positions shift to higher energy region with the x value of the $Pr_{1-x}Ca_xMnO_{3-y}$ system, which means the increase of Mn^{4+} ion content or the mixed valency state between Mn^{3+} and Mn^{4+} ions. Two different absorption peaks appear in the energy region of 6547–6558 eV, which peaks correspond to the dipole-allowed 1s $\rightarrow$ 4p main transitions of the Mn atoms and also to 1s $\rightarrow$ 4p transition followed by the shakedown process of ligand to metal charge transfer (LMCT).

All the compounds are shown nonstoichiometric compositions in the oxygen vacancy range of –0.046 to 0.299 from the iodometric titration. The content of Mn^{4+} ion has been determined by the iodometry in the range of 0.042–0.438. Thus the nonstoichiometric chemical formulas of the $Pr_{1-x}Ca_xMn^{3+}_{1-\tau}Mn^{4+}_{\tau}O_{3-y}$ compounds have been obviously formulated.

The $Pr_{1-x}Ca_xMnO_{3-y}$ compounds for the compositions of $x = 0.4$, 0.6, and 0.8 show the transition from antiferromagnetic to paramagnetic state. However, the $Pr_{1-x}Ca_xMnO_{3-y}$ compounds of $x = 0.0$, 0.2, and 1.0 show the transition from ferromagnetic to paramagnetic state. The double exchanges competitive with the super-exchange have observed in the $Pr_{1-x}Ca_xMnO_{3-y}$ system.

The magnetic transition temperature is related with the content of Mn^{4+} ions in the sample. The higher amounts of Mn^{4+} ions have been led to the higher transition temperature. The spin states of Mn ions have been calculated from the paramagnetic part of SQUID patterns. High spin state of Mn^{4+} and low spin state of Mn^{3+} ions of the $Pr_{1-x}Ca_xMnO_{3-y}$ system have been identified.

The electrical conductivity shows typical semiconducting behavior and the charge ordering transitions have also been observed. The transition temperature increases with the decreasing Mn–O bond length and also shows higher value under the magnetic field than that under zero magnetic fields.

The MR ratios show both positive and negative values due to the competitive relationship between the carrier bending and the spin ordering processes. The larger MR ratios have been observed in the sample

with low activation energy in good agreement with competitive process between the carrier bending and the spin ordering simultaneously.

Acknowledgements This work was supported by Korea Research Foundation Grant (KRF-2000-015-DP0200). The X-ray absorption experiments at PLS were supported in part by MOST and POSCO.

References

1. Kohler M (1938) Ann Phys 32:211
2. Volger J (1954) Physica (Utrecht) 20:49
3. Baibich MN, Broto JM, Fert A, Nguyen Van Dau F, Petroff F, Etienne P, Creutzet G, Friederich A (1988) J Phys Rev Lett 61:2472
4. Parkin SSP, More N, Roche KP (1990) Phys Rev Lett 64:2304
5. Chahara K, Ohno T, Kasai M, Kozono Y (1993) Appl Phys Lett 63:1990
6. Jin S, McCormack M, Tiefel TH, Ramesh R (1994) J Appl Phys 76:6929
7. Von Helmolt R, Wecker J, Samwer K, Haupt L, Barner K (1994) J Appl Phys 76:6925
8. Ushibara A, Moritomo Y, Arima T, Asamitsu A, Kido G, Tokura Y (1995) Phys Rev B 51:14103
9. Mahendiran R, Tiwary SK, Raychaudhuri AK, Ramakrishnan TV, Mahesh R, Rangavittal N, Rao CNR (1996) Phys Rev B 53:3348
10. Paul Attfield J (1998) Chem Mater 10:3239
11. Majumda P, Littlewood PB (1998) Nature 395:479
12. Manyala N, Sidis Y, Ditusa JF, Aeppli G, Young DP, Fisk A (2000) Nature 404:581
13. Yin RZ (2002) Dissertation for PhD Degree, Yonsei University, South Korea, 53 pp
14. Rao CNR, Gopalakrishnan J (1997) New directions in solid state chemistry. Cambridge University press, Cambridge, New York, Melbourne, p 28
15. Jonker GH, Van Santen JH (1953) Physica 19:120
16. Yin RZ, Park JW, Choi HN, Oh SK, Yo CH (2004) Mater Chem Phys 86:137
17. Laplume J (1955) L'onde Electrique 335:113
18. Jaime M, Salamon MB, Robinstein M, Treece RE, Horwitz JS, Chrisey DB (1996) Phys Rev B 54:11914